

Chiral supersolid and dissipative time crystal in Rydberg-dressed Bose-Einstein condensates with Raman-induced spin-orbit coupling

Xianghua Su, Xiping Fu, Yang He, Ying Shang, Kaiyuan Ji, and Linghua Wen*

*Hebei Key Laboratory for Microstructural Material Physics,
School of Science, Yanshan University, Qinhuangdao 066004, China*

(Dated: January 14, 2025)

Spin-orbit coupling (SOC) is one of the key factors that affect the chiral symmetry of matter by causing the spatial symmetry breaking of the system. We find that Raman-induced SOC can induce a chiral supersolid phase with a helical antiskyrmion lattice in balanced Rydberg-dressed two-component Bose-Einstein condensates (BECs) in a harmonic trap by modulating the Raman coupling strength, strong contrast with the mirror symmetric supersolid phase containing skyrmion-antiskyrmion lattice pair for the case of Rashba SOC. Two ground-state phase diagrams are presented as a function of the Rydberg interaction strength and the SOC strength, as well as that of the Rydberg interaction strength and the Raman coupling strength, respectively. It is shown that the interplay among Raman-induced SOC, soft-core long-range Rydberg interactions, and contact interactions favors rich ground-state structures including half-quantum vortex phase, stripe supersolid phase, toroidal stripe phase with a central Anderson-Toulouse coreless vortex, checkerboard supersolid phase, mirror symmetric supersolid phase, chiral supersolid phase and standing-wave supersolid phase. In addition, the effects of rotation and in-plane quadrupole magnetic field on the ground state of the system are analyzed. In these two cases, the chiral supersolid phase is broken and the ground state tends to form a miscible phase. Furthermore, the stability and superfluid properties of the two-component BECs with Raman-induced SOC and Rydberg interactions in free space are revealed by solving the Bogoliubov-de Gennes equation. Finally, we demonstrate that when the initial state is a chiral supersolid phase the rotating harmonic trapped system sustains dissipative continuous time crystal by studying the rotational dynamic behaviors of the system.

I. INTRODUCTION

Supersolid is an exotic quantum state of matter possessing simultaneously a superfluid nature and the translational symmetry-breaking feature of solid structures [1, 2]. The initial exploration of supersolids mainly focused on helium, but these studies of solid ^4He at low temperature ultimately did not find conclusive evidence of supersolidity [3–5]. Recently, Bose-Einstein condensates (BECs), as an excellent candidate for studying supersolid due to their extremely high purity and full experimental controllability, have attracted a great deal of attention. Relevant experimental and theoretical investigations have shown that the supersolid can be realized in ultracold atomic BECs by spin-orbit coupling (SOC) [6, 7], dipole-dipole interaction (DDI) [8–13], optical lattices [14, 15] or Rydberg dressing [16–21]. For instance, Ketterle group observed a stripe supersolid phase in spin-orbit coupled BECs, and the continuous translational symmetry of the system was broken in the x direction of free space [6]. In a dipolar BEC, the partially attractive nature of the DDI tends to make the system unstable towards a collapse, while the repulsive interaction induced by quantum fluctuations can stabilize the system and lead to the formation of stable quantum droplets [22–25]. The quantum droplets may form supersolid under the appropriate conditions [8–10, 25–27], where the spon-

aneous periodic density modulation is accompanied by the phase coherence between the droplets. For trapped quasi-one-dimensional (quasi-1D) and quasi-2D dipolar BECs, the dipolar supersolids appear in various spatially-periodic arrangements of droplets, such as straight-line pattern, triangular lattice, square lattice, hexagonal lattice and honeycomb lattice [10, 28–30]. The physical systems mentioned above are hard-core systems, where the interatomic contact interaction or long-range DDI is essentially a hard-core interaction. By comparison, the Rydberg interactions (van der Waals interactions) in Rydberg-dressed BECs are soft-core isotropic long-range interactions. The strong van der Waals interactions are expected to break the spatial translational symmetry in multiple directions and induce the formation of 2D and 3D supersolids [16, 19].

On the other hand, spin-orbit coupling is an interaction between the spin and the momentum of a quantum particle, which breaks the spatial symmetry and the Galilean invariance, thus favoring many novel quantum states for ultracold Bose gases [31, 32], such as plane-wave phase [32], stripe phase [33, 34], supersolid phase [6, 35], lattice phase [36], checkerboard phase [37], various vortex states [38–40], soliton excitation [41, 42] and skyrmion [43]. Based on the symmetry of interaction, there exist three typical types of 2D SOC in condensate systems, including Rashba SOC [44], Dresselhaus SOC [45] and Rashba-Dresselhaus SOC [46]. Recent studies show that the combined effects of SOC and nonlocal soft-core long-range interactions can induce the formation of rich quantum phases [47–50]. In particular, the Rashba SOC or Dresselhaus SOC is predicted to achieve the symmetry

*Electronic address: linghuawen@ysu.edu.cn

breaking of chirality and lead to a chiral supersolid in Rydberg-Dressed BECs [48, 50]. In the latest years, increasing attention has been paid to the study of chiral matter, which provides new ideas for the design of new materials [51–54].

In addition, 1D, 2D and 3D Raman-induced SOC in atomic BECs have been implemented experimentally by Raman coupling that flips atomic pseudospins and transfers linear momentum simultaneously [31, 55, 56]. Compared with the Rashba SOC and Dresselhaus SOC, the Raman-induced SOC suppresses the low-energy density of state, and results in the nonmonotonic behavior of the low-energy density of state as a function of the Raman coupling strength. The change in Raman coupling strength can break spatial symmetry [32], but it is not yet clear whether it will lead to the emergence of chiral supersolid. Furthermore, spontaneous time symmetry breaking may lead to an exotic dynamical phase, the time crystal [57–61]. Previous studies have shown that time crystal can be observed in a variety of physical systems, such as Floquet many-body localized (Floquet-MBL) system [62], dipolar many-body system [63], dissipative atom-cavity BEC system [64], and Rydberg gas [65]. Whether the time-reversal symmetry breaking caused by spin-orbit coupling can lead to the formation of time crystals is an issue worth exploring.

In this paper, we consider quasi-2D two-component BECs with Raman-induced SOC and balanced Rydberg interactions in a harmonic trap. Two ground-state phase diagrams are given. Due to the combined effects of Raman-induced SOC, Rydberg interactions and contact interactions, the system sustains rich ground-state structures including half-quantum vortex phase, stripe supersolid phase, toroidal stripe phase with a central Anderson-Toulouse coreless vortex, checkerboard supersolid phase, standing-wave supersolid phase, mirror-symmetric supersolid phase with skyrmion-antiskyrmion lattice pair, and chiral supersolid phase with a helical antiskyrmion lattice, which can be realized by modulating the Rydberg interaction strength, SOC strength, and Raman coupling strength. Additionally, it is shown that rotation and in-plane gradient magnetic field can lead to the destruction of the chiral supersolid phase and transform the ground state of the system into a miscible phase. Furthermore, we obtain the Bogoliubov excitation spectra of the quasi-2D two-component BECs with Raman-induced SOC and Rydberg interactions in free space by numerically solving the Bogoliubov de Gennes equation. The stability features and superfluid properties of the system are analyzed. Intriguingly, we find that for strong Rydberg interactions the two branches of the excitation spectra along the x axis contact with each other at two points. Moreover, we investigate the rotating dynamics of the system by using a phenomenological dissipation model, and find that the system supports dissipative continuous time crystals.

This paper is organized as follows. In Sec. II, we formulate the theoretical model and methods. In Sec.

III, we first study the ground-state structures of the system, and then discuss the effects of rotation and in-plane quadrupole magnetic field on the ground state of the system. Next, the Bogoliubov excitations of the two-component Rydberg-dressed BECs with Raman-induced SOC in free space are analyzed. Furthermore, we investigate the rotational dynamic behaviors of the system. Finally, we briefly discuss the experimental feasibility of the present system. The main conclusions of the paper are summarized in the last section.

II. THEORETICAL MODEL

We consider a quasi-2D Raman-induced spin-orbit coupled spin-1/2 BEC with Rydberg interactions in a harmonic trap. Under the mean-field approximation, the energy functional of the system is given by [16, 19, 32, 48]

$$\begin{aligned}
 E = & \int d\mathbf{r} \psi^\dagger \left[-\frac{\hbar^2}{2m} \nabla^2 + V(\mathbf{r}) + v_{so} \right] \psi \\
 & + \frac{1}{2} \int d\mathbf{r} \sum_{j,l=1,2} g_{jl} \psi_j^*(\mathbf{r}) \psi_l^*(\mathbf{r}) \psi_l(\mathbf{r}) \psi_j(\mathbf{r}) \\
 & + \frac{1}{2} \int d\mathbf{r} d\mathbf{r}' \sum_{j,l=1,2} \psi_j^*(\mathbf{r}) \psi_l^*(\mathbf{r}') \\
 & \times U_{jl}(\mathbf{r} - \mathbf{r}') \psi_l(\mathbf{r}') \psi_j(\mathbf{r}), \quad (1)
 \end{aligned}$$

where m is the atomic mass, $\psi = [\psi_1(\mathbf{r}), \psi_2(\mathbf{r})]^T$ with $\mathbf{r} = (x, y)$, ψ_j ($j = 1, 2$) is the component wave function, with 1 and 2 corresponding to spin-up (component 1) and spin-down (component 2), respectively. The system satisfies the normalization condition $\int d\mathbf{r} (|\psi_1|^2 + |\psi_2|^2) = N$. $V(\mathbf{r}) = m\omega_\perp^2(x^2 + y^2)/2$ is the 2D external trapping potential with the radial trap frequency ω_\perp . We assume that the system is tightly confined by a harmonic trap in the z direction to form a quasi-2D system with frequency ω_z and characteristic length $a_z = \sqrt{\hbar/m\omega_z}$. The coefficients $g_{jj} = 2\sqrt{2\pi}a_j\hbar^2/ma_z$ ($j = 1, 2$) and $g_{12} = g_{21} = 2\sqrt{2\pi}a_{12}\hbar^2/ma_z$ represent the intra- and interspecies coupling strengths, where a_j and a_{12} are the s -wave scattering lengths between intra- and intercomponent atoms. The Raman-induced SOC reads

$$v_{so} = -i\hbar\kappa(\sigma_x\partial_x + \sigma_y\partial_y) + \frac{\Omega_R}{2}\sigma_z - \frac{\delta}{2}\sigma_x, \quad (2)$$

where $\boldsymbol{\sigma} = (\sigma_x, \sigma_y, \sigma_z)$ are the Pauli matrices, κ is the SOC strength, Ω_R is the Raman coupling strength, and δ is the detuning. In the mean time, the soft-core long-range interaction potential, i.e., the nonlocal Rydberg interaction potential, can be expressed as [16, 19]

$$U_{jl}(\mathbf{r} - \mathbf{r}') = \frac{\tilde{C}_6^{jl}}{R_6^c + |\mathbf{r} - \mathbf{r}'|^6}. \quad (3)$$

Here we assume that the system has equilibrium Rydberg interactions for $\tilde{C}_6^{11} = \tilde{C}_6^{12} = \tilde{C}_6^{21} = \tilde{C}_6^{22} = \tilde{C}_6$. $\tilde{C}_6 =$

$(\Omega/2\Delta)^4 C_6/\sqrt{2\pi}a_z$ with the Rabi frequency Ω and the laser detuning Δ , $R_c = (C_6/2\hbar\Delta)^{1/6}$ is blockade radius, and C_6 is the strength of the van der Waals interaction between Rydberg atoms.

For the sake of numerical simulation and calculation, we introduce the notations $\tilde{t} = t/\tau$, $\tilde{\mathbf{r}} = \mathbf{r}/R_c$, $\omega_c = \omega_\perp\tau$, $\tilde{\Omega}_R = \Omega_R\tau/\hbar$, $\tilde{\delta} = \delta\tau/\hbar$, $\tilde{\kappa} = \kappa\tau/R_c$, $\tilde{\psi}_j = \sqrt{R_c^3/N}\psi_j$ ($j = 1, 2$), $\tilde{U}_{jl}(\mathbf{r} - \mathbf{r}') = mN\tilde{C}_6^{jl}/\hbar^2 R_c^6(1 + |\tilde{\mathbf{r}} - \tilde{\mathbf{r}}'|^6)$, and $\tau = R_c^2 m/\hbar$, where the blockade radius R_c and τ are chosen as the length and time scales. Then we obtain the dimensionless 2D coupled GP equations

$$i\frac{\partial\psi_1(\mathbf{r})}{\partial t} = \left[-\frac{1}{2}\nabla^2 + V(\mathbf{r}) + \beta_{11}|\psi_1(\mathbf{r})|^2 + \beta_{12}|\psi_2(\mathbf{r})|^2 + \frac{\Omega_R}{2} + \int U_{11}(\mathbf{r} - \mathbf{r}')|\psi_1(\mathbf{r}')|^2 d\mathbf{r}' + \int U_{12}(\mathbf{r} - \mathbf{r}')|\psi_2(\mathbf{r}')|^2 d\mathbf{r}' \right] \psi_1(\mathbf{r}) - \kappa(i\partial_x + \partial_y)\psi_2(\mathbf{r}) - \frac{\delta}{2}\psi_2(\mathbf{r}), \quad (4)$$

$$i\frac{\partial\psi_2(\mathbf{r})}{\partial t} = \left[-\frac{1}{2}\nabla^2 + V(\mathbf{r}) + \beta_{22}|\psi_2(\mathbf{r})|^2 + \beta_{21}|\psi_1(\mathbf{r})|^2 - \frac{\Omega_R}{2} + \int U_{22}(\mathbf{r} - \mathbf{r}')|\psi_2(\mathbf{r}')|^2 d\mathbf{r}' + \int U_{21}(\mathbf{r} - \mathbf{r}')|\psi_1(\mathbf{r}')|^2 d\mathbf{r}' \right] \psi_2(\mathbf{r}) - \kappa(i\partial_x - \partial_y)\psi_1(\mathbf{r}) - \frac{\delta}{2}\psi_1(\mathbf{r}), \quad (5)$$

where the tildes are omitted for brevity. The dimensionless 2D harmonic potential can be written as $V(\mathbf{r}) = \omega_c^2(x^2 + y^2)/2$ with the strength of the radius potential ω_c . The dimensionless intra- and interspecies interaction strengths read as $\beta_{jj} = 2\sqrt{2\pi}a_j N/R_c a_z$ ($j = 1, 2$) and $\beta_{12} = \beta_{21} = 2\sqrt{2\pi}a_{12} N/R_c a_z$. For convenience, we rescale the soft-core long-range Rydberg interaction strength as $mN\tilde{C}_6/\hbar^2 R_c^6$ and denote it as \tilde{C}_6 .

To further explore the topological properties of the system, we adopt a nonlinear Sigma model [40, 66] and introduce a normalized complex-valued spinor $\boldsymbol{\chi} = [\chi_1, \chi_2]^T$ with $|\chi_1|^2 + |\chi_2|^2 = 1$. The corresponding two-component wave functions are given by $\psi_1 = \sqrt{\rho}\chi_1$ and $\psi_2 = \sqrt{\rho}\chi_2$, where $\rho = |\psi_1|^2 + |\psi_2|^2$ is the total density of the system. The spin density is defined as $\mathbf{S} = \bar{\boldsymbol{\chi}}\boldsymbol{\sigma}\boldsymbol{\chi}$, and the components of \mathbf{S} are written as

$$S_x = \chi_1^*\chi_2 + \chi_2^*\chi_1, \quad (6)$$

$$S_y = i(\chi_2^*\chi_1 - \chi_1^*\chi_2), \quad (7)$$

$$S_z = |\chi_1|^2 - |\chi_2|^2, \quad (8)$$

with $|\mathbf{S}|^2 = S_x^2 + S_y^2 + S_z^2 = 1$. The spacial distribution of the topological structure of the system can be well characterized by the topological charge density

$$q(\mathbf{r}) = \frac{1}{4\pi}\mathbf{S} \cdot \left(\frac{\partial\mathbf{S}}{\partial x} \times \frac{\partial\mathbf{S}}{\partial y} \right), \quad (9)$$

and the topological charge Q is given by

$$Q = \int q(\mathbf{r}) dx dy. \quad (10)$$

III. RESULTS AND DISCUSSION

A. Chiral supersolid and phase diagram

By numerically solving the 2D coupled GP equations (4)-(5) and minimizing the GP energy functional of the system, we can obtain the ground state of the system. In our simulation, we fix the Rydberg blockade radius $R_c = 1.5$, $\omega_c = 5$ and $\delta = 0$, and assume that the intra- and interspecies interaction strengths are $\beta_{11} = \beta_{22} = 100$ and $\beta_{12} = 200$, respectively. In the presence of Rashba SOC or Dresselhaus SOC, it has been reported that the unbalanced intra- and intercomponent Rydberg interactions can induce a chiral supersolid (CSS) phase in homogeneous two-component BECs [48]. In the CSS phase, the chiral symmetry of the system is broken and the periodic density modulation is spontaneously formed. In our work, we first consider the simple case of $\Omega_R = 0$ in which the Raman-induced SOC becomes the Rashba SOC. Under the condition of equilibrium Rydberg interactions, the typical density distributions, phase distributions and spin texture of the system are shown in Fig. 1(a), where the system exhibits a phase separated and periodically density modulated structure and features a mirror symmetry. At the same time, there exists a singular topological structure, where the visible vortices (clockwise rotation) are generated in the upper half space of component 1 while the visible antivortices (anticlockwise rotation) are created in the lower half space of component 2 (see the density and phase distributions in Fig. 1(a)). According to the distribution of the visible vortices, it can be seen that the superfluid is a local current. Therefore, we can call the phase as mirror symmetric supersolid (MSSS) phase. From the spin texture in Fig. 1(a), there is a skyrmion lattice in the $y < 0$ region, with the local topological charge of each skyrmion being $Q = 1$ [67, 68], and there is an antiskyrmion lattice in the $y > 0$ region, with the local topological charge of each antiskyrmion being $Q = -1$. The skyrmion lattice and the antiskyrmion lattice are symmetrically distributed about the $y = 0$ axis, forming skyrmion-antiskyrmion lattice pair. In addition, a spin Neel domain wall is generated along the $y = 0$ direction.

Next, we study the case of Raman-induced SOC, i.e., the case of nonzero Ω_R . Intriguingly, we obtain a chiral supersolid phase by using the Raman-induced SOC with the equilibrium Rydberg interactions as shown in Fig. 1(b). By comparison, the two spin components in this quantum phase are separated along the radial direction in each unit cell possessing a clockwise circulation, where component 2 is located in the center and surrounded by component 1. In the meantime, the antivortices in com-

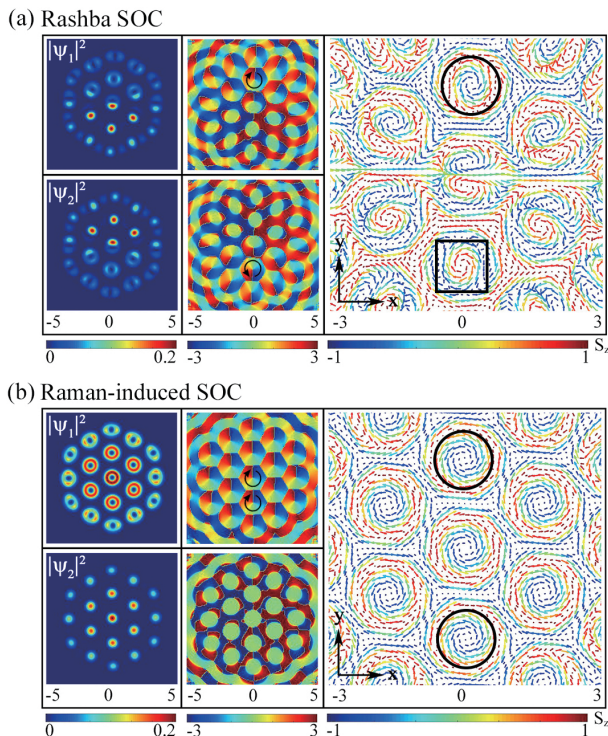


FIG. 1: (Color online) Typical density distribution (left), phase distribution (middle) and spin texture (right) of the system for (a) $\tilde{C}_6 = 1500$, $\kappa = 4$, $\Omega_R = 0$ and (b) $\tilde{C}_6 = 1500$, $\kappa = 4$, $\Omega_R = 10$. The arrows in the spin texture represent the transverse spin vector (S_x , S_y) and the color of each arrow indicates the magnitude of S_z . The square and circle in the spin texture denote a skyrmion and an antiskyrmion, respectively. Here each panel is a square, and the range and scale of the vertical axis are the same as those of the horizontal axis. The unit length is R_c .

ponent 2 disappear, while all the phase defects in component 1 become visible vortices and constitute a triangular vortex lattice containing local and global circulating particle currents. Obviously, the chiral symmetry of the system is broken. Furthermore, our computation results demonstrate that the local topological defects in the spin texture in Fig. 1(b) are helical antiskyrmions [69] with topological charge $Q = -1$, thus the spin texture in Fig. 1(b) is an exotic helical antiskyrmion lattice, where the spin Neel domain wall spontaneously vanishes. These results indicate that the Raman laser leads to the reversal of certain local spin structures. Compared with Ref. [48], here the novel chiral supersolid phase with helical antiskyrmion lattice can be created in two-component BECs with Raman-induced SOC and balanced Rydberg interactions in a harmonic trap, merely by adjusting the Raman coupling strength. Therefore the present system is more approach to the actual harmonic-trapped BEC system and relatively easier to achieve.

In order to further elucidate the ground-state properties of the system, we provide two ground-state phase diagrams with respect to \tilde{C}_6 and κ and with respect to

\tilde{C}_6 and Ω_R as shown in Figs. 2(a) and 2(b), respectively. The typical density distributions, phase distributions and momentum distributions of various ground-state phases are given in Fig. 2(c). From Fig. 2(a), for the weak Rydberg interaction \tilde{C}_6 with fixed Raman coupling strength Ω_R , the system sustains half-quantum vortex (HQV) phase and stripe supersolid (SSS) phase, depending on the SOC strength. With the increase of SOC strength, the ground state of the system changes from the HQV phase to the SSS phase. In the HQV phase, the momentum distribution is concentrated at a central discrete point near the origin of the momentum space, which means that the atoms are essentially condensed at zero momentum (see Fig. 2(c)(I)). Unlike the HQV phase, the momentum distribution of the SSS phase exhibits two discrete high-density points symmetrically distributed on the positive and negative half axes of the k_y axis, respectively (see Fig. 2(c)(II)). This indicates that the atoms in the SSS phase are principally condensed at two finite momenta. However, for fixed SOC strength but stronger Rydberg interaction, the two component densities form spatially separated and multiple concentric layered toroidal stripes, and the central vortex core of component 1 is filled by the nonrotating component 2 as shown in Fig. 2(c)(III). We may call this phase as toroidal stripe (TS) phase with a central Anderson-Toulouse coreless vortex [70]. At the same time, the momentum distribution displays an obvious high-density ring and two low-density rings. For the case of strong SOC, with the further increase of the Rydberg interaction strength, the ground state of the system evolves from the TS phase into the checkerboard supersolid (CBSS) phase (Fig. 2(c)(IV)), where the density peaks form a regular checkerboard pattern, and many hidden vortex-antivortex pairs are generated in each component [71–73]. The corresponding momentum distribution is focused on four high density points and some low density points along a ring. Whereas for the case of weak (or relatively weak) SOC and strong Rydberg interaction, the system tends to form the chiral supersolid (CSS) phase with a helical antiskyrmion lattice (see Fig. 1(b), Fig. 2(a) and Fig. 2(c)(VI)), where the momentum distribution is mainly concentrated at seven discrete high-density points constituting a triangular lattice.

When both the Rydberg interaction and the SOC are strong, the CSS phase transforms into the standing-wave supersolid (SWSS) phase as shown in Fig. 2(a) and Fig. 2(c)(VII), where the momentum distribution becomes a ring structure composed of stripe density standing waves. Physically, for the SSS phase, CBSS phase and SWSS phase, the translation symmetry of the system is broken due to the strong SOC, resulting in the formation of a supersolid crystal structure of density modulation.

In the phase diagram as the function of \tilde{C}_6 and Ω_R , we find that in the region composed of strong Rydberg interaction ($\tilde{C}_6 \gtrsim 1000$) and weak Raman coupling, the system supports the MSSS phase with skyrmion-antiskyrmion lattice pair (see Fig. 2(b) and Fig. 2(c)(V)).

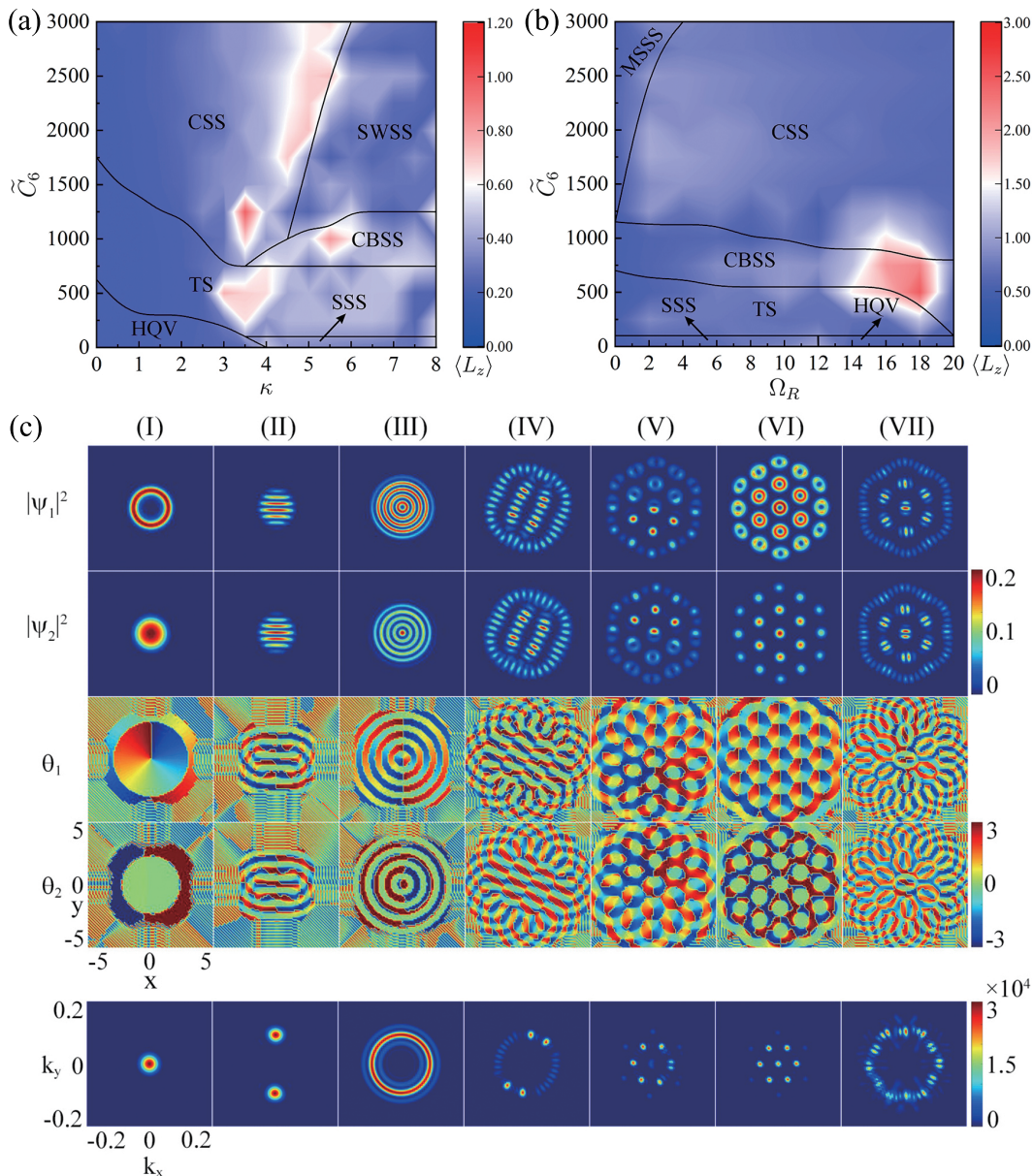


FIG. 2: (Color online) (a) Ground-state phase diagram as the function of the SOC strength κ and the Rydberg interaction strength \tilde{C}_6 for Rydberg-dressed two-component BECs with Raman-induced SOC, where the Raman coupling strength $\Omega_R = 10$. (b) Ground-state phase diagram with respect to Ω_R and \tilde{C}_6 , where $\kappa = 4$. The background color in (a) and (b) indicates the magnitude of $\langle L_z \rangle$. (c) The first four rows denote typical density distributions and phase distributions of various ground-state phases, where (I)-(VII) correspond to the half-quantum vortex (HQV) phase, stripes supersolid (SSS) phase, toroidal stripe (TS) phase with a central Anderson-Toulouse coreless vortex, checkerboard supersolid (CBSS) phase, mirror-symmetric supersolid (MSSS) phase with skyrmion-antiskyrmion lattice pair, chiral supersolid (CSS) phase with a helical antiskyrmion lattice, and standing-wave supersolid (SWSS) phase, respectively. The last row corresponds to the momentum distribution of the system. The relevant parameters are (I) $\tilde{C}_6 = 10$, $\kappa = 2$, $\Omega_R = 10$, (II) $\tilde{C}_6 = 10$, $\kappa = 6$, $\Omega_R = 10$, (III) $\tilde{C}_6 = 250$, $\kappa = 6$, $\Omega_R = 10$, (IV) $\tilde{C}_6 = 1000$, $\kappa = 6$, $\Omega_R = 10$, (V) $\tilde{C}_6 = 1500$, $\kappa = 4$, $\Omega_R = 0$, (VI) $\tilde{C}_6 = 1500$, $\kappa = 4$, $\Omega_R = 10$, and (VII) $\tilde{C}_6 = 1500$, $\kappa = 7$, $\Omega_R = 10$. The unit length is R_c .

The density of MSSS phase in k -space is chiefly concentrated at a few irregular discrete points. With the increase of Raman coupling strength, the ground-state phase of the system changes from the MSSS phase to the CSS phase with a helical antiskyrmion lattice. Similarly,

there also exist HQV phase, SSS phase, TS phase, and CBSS phase in the phase diagram of Fig. 2(b).

Moreover, the average orbital angular momentum (i.e., canonical angular momentum) per atom, $\langle L_z \rangle = \sum_{j=1,2} \int d\mathbf{r} \psi_j^* (x p_y - y p_x) \psi_j$ [38], can also show the

influence of the SOC strength, Rydberg interaction strength, and Raman coupling strength on the ground-state structure and phase transition of the system. The dependence of $\langle L_z \rangle$ on κ , \tilde{C}_6 , and Ω_R is displayed in Figs. 2(a) and 2(b), which indicates that there is no simple linear relationship, but a complex correlation associated with the specific ground-state configurations. For instance, the strong SOC overall leads to more angular momentum in the system due to the interaction between the spin and the momentum except for the SWSS phase (see Fig. 2(a)). Near the boundary between the CSS phase and the SWSS phase in the region of strong SOC and strong Rydberg interaction, there is a significant sudden change in the average orbital angular momentum per atom. The physical reason is that in the CSS phase there are a large number of visible vortices carrying evident angular momentum while in the SWSS phase the system forms multiple localized stripe structures with almost no phase defects. However, for the CSS phase, $\langle L_z \rangle$ decreases slightly as the Raman coupling strength Ω_R increases (see Fig. 2(b)). This behavior is due to the presence of a small amount of hidden vortices [71–73] in component 2 for the case of small Raman coupling strength. In short, the comprehensive competition of Rydberg interaction, SOC, and Raman coupling leads to complicated changes in the orbital angular momentum.

As mentioned above, the significant differences in the structure and momentum distribution of these exotic quantum phases (especially the novel MSSS phase with skyrmion-antiskyrmion lattice pair and chiral supersolid phase with a helical antiskyrmion lattice) in the harmonic trapped BECs with Raman-induced SOC and equilibrium Rydberg interactions allow them relatively easy to be observed and verified in the future experiments.

B. Destruction of chiral supersolid

Next, we illustrate the effects of two commonly used regulation schemes in experiments, namely rotating the system and applying an in-plane quadrupole magnetic field, on the ground-state properties of the system. The results show that the two schemes break the CSS phase of the system and lead to the formation of novel quantum phases. For the first case, we consider a rotating system in a rotating frame by adding the term $-\Omega_r L_z \psi_1(\psi_2)$ to the right sides of the GP equations (4) and (5) with the rotation frequency Ω_r . The rapid rotation ($\Omega_r = 0.8$) of the external potential breaks the original chiral supersolid structure (see Fig. 3(a), Fig. 1(b), and Fig. 2(VI)), where the original visible vortices outside the central region in component 1 disappear, and the density of component 1 exhibits periodic modulation along the azimuth direction, accompanied by the creation of double-layer hidden antivortex necklaces in both components. At the same time, the original helical antiskyrmion lattice in Fig. 1(b) is broken, and only one con-

ventional antiskyrmion is generated at the center. Thus the ground state of the rotating system for large rotation frequency forms a special annular supersolid phase with double-layer hidden antivortex necklaces and a central Anderson-Toulouse coreless vortex.

For the second case, we apply an in-plane quadrupole magnetic field (i.e., an in-plane gradient magnetic field) to the system by adding the term $g_F \mu_B \mathbf{B}(\mathbf{r}) \cdot \boldsymbol{\sigma}$ to the single-particle Hamiltonian [74, 75]. Here $g_F = -1/2$ is the Lande factor, μ_B is Bohr magnetic moment, $\mathbf{B}(\mathbf{r}) = B(x\hat{e}_x - y\hat{e}_y)$ is the in-plane gradient magnetic field with the strength B , and $\boldsymbol{\sigma}$ is the 2×2 Pauli spin matrices. Once the in-plane quadrupole magnetic field is included, e.g., $B = 6$ as shown in Fig. 3(b), the system exhibits an unusual density and phase distributions. Due to the presence of the in-plane quadrupole magnetic field, the density distributions of the two components are symmetrical about the two principal diagonals. In the meantime, the phase distributions of two components display typical quadrupole field characteristics, with hidden vortices and antivortices occupying the two principal diagonals, respectively. Particularly, the phase defects along the two principal diagonals in component 2 constitute a series of hidden vortex-antivortex pairs with each other. Accordingly, the ground state of the system becomes a droplet lattice state with hidden vortices and antivortices along two principal diagonals. This ground-state structure is different from the case of spin-orbit coupled dipolar BECs with in-plane quadrupole magnetic field (see Figs. 1(d) and 1(g) in Ref. [75]), where the ground state is an annular structure with hidden vortex-antivortex cluster in the central density hole region. In addition, our computation results show that the local topological charges in the spin texture in Fig. 3(b) approach $Q = 1$ (square marks), $Q = 0.5$ (pentagon marks), and $Q = -0.5$ (hexagon marks), which indicates that the local topological defects are skyrmion, half-skyrmion (meron), and half-antiskyrmion (antimeron), respectively [68]. Hence the spin texture forms a complex skyrmion-meron-antimeron cluster with the topological defects being distributed along the two principal diagonals.

Furthermore, the changes in the ground-state structure of the system for the above two cases can also be reflected by the miscibility of the two components. A miscibility parameter η can be defined to approximately measure the degree of overlap between the densities of the two components [76, 77],

$$\eta = 2 \int d\mathbf{r} |\psi_1| |\psi_2| = 2 \int d\mathbf{r} \sqrt{|\psi_1|^2 |\psi_2|^2}. \quad (11)$$

This expression means that $\eta = 1$ for the complete overlap between the two densities, and η decreases as the overlap diminishes. In the absence of rotation and gradient magnetic field, the CSS phase shows a clear spatial separation for the two components (see Fig. 1(b)), and the miscibility parameter η has the smallest value as shown in Figs. 3(c) and 3(d). With the increase of the rotation frequency Ω_r or the quadrupole magnetic

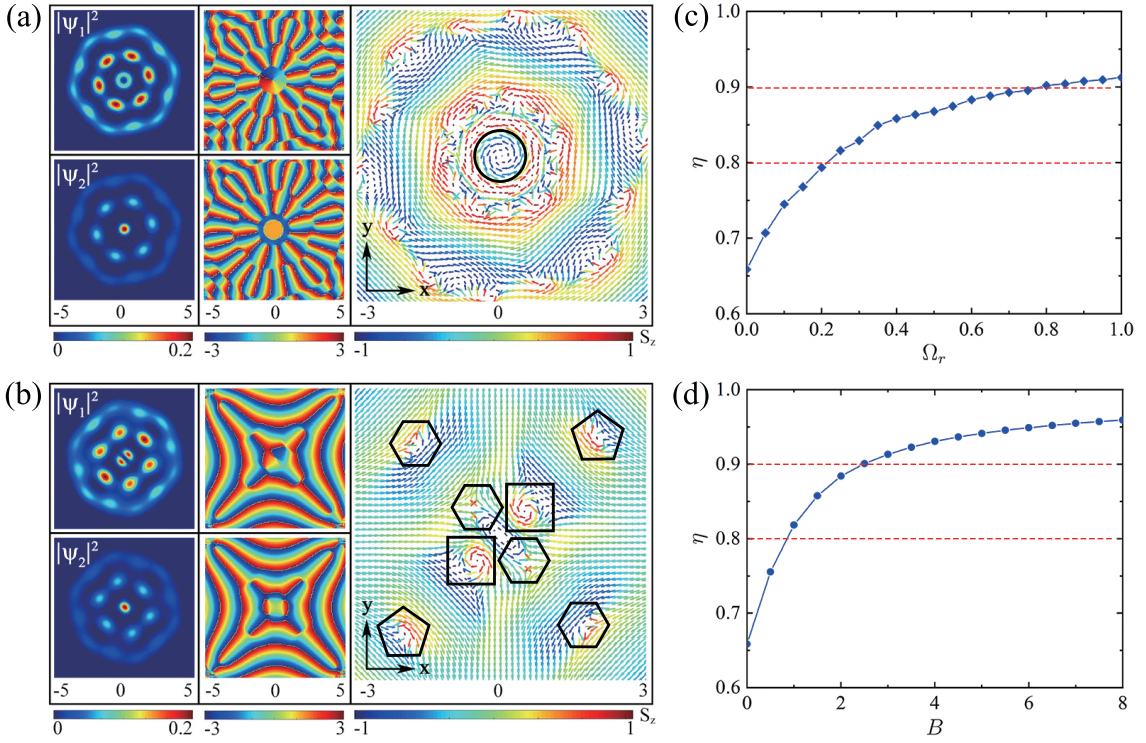


FIG. 3: (Color online) (a) Ground-state density distribution, phase distribution and spin texture of rotating two-component BECs with Raman-induced SOC and Rydberg interactions, where the rotation frequency $\Omega_r = 0.8$, $\tilde{C}_6 = 1500$, $\kappa = 4$, and $\Omega_R = 10$. (b) Ground-state density distribution, phase distribution and spin texture of non-rotating two-component BECs with Raman-induced SOC and Rydberg interactions in an in-plane quadrupole magnetic field, where the quadrupole field strength $B = 6$, $\tilde{C}_6 = 1500$, $\kappa = 4$, and $\Omega_R = 10$. The arrows in the spin texture represent the transverse spin vector (S_x , S_y) and the color of each arrow indicates the magnitude of S_z . The square, circle, pentagon, and hexagon in the spin texture denote a skyrmion, an antiskyrmion, a half-skyrmion, and a half-antiskyrmion, respectively. Here each panel in (a) and (b) is a square, and the range and scale of the vertical axis are the same as those of the horizontal axis. The unit length is R_c . (c) and (d) The miscibility η as a function of Ω_r and B for $\tilde{C}_6 = 1500$, $\kappa = 4$, and $\Omega_R = 10$, respectively.

field strength B , the system gradually changes from an immiscible phase to a miscible phase in which $\eta \gtrsim 0.8$ [76, 77]. As the parameter Ω_r or B further increases, the system becomes more miscible and eventually approaches a stable value. In particular, for the case of in-plane quadrupole magnetic field, the miscibility of the system achieves a greater value of $\eta > 0.95$. This is due to fact that the strong magnetic field destroys the original visible vortex structure including the visible vortex at the center in component 1, resulting in the generation of hidden vortices and antivortices in both components, as well as the high overlap of some hidden vortices and antivortices in both components.

C. Bogoliubov excitations

It is extremely difficult to study the collective excitations of the interacting two-component BECs with Raman-induced SOC and Rydberg interactions in a 2D harmonic trap. Below we just discuss the Bogoliubov excitations of the present system in free space (i.e., in the

absence of external trapping potential). Applying a local approximation, the Rydberg interaction term in the GP equations (4) and (5) can be approximated as [18]

$$\begin{aligned} \tilde{C}_6 \int \frac{|\psi_{1,2}(\mathbf{r} - \mathbf{r}')|^2}{1 + r'^6} d\mathbf{r}' &\approx \tilde{C}_6 |\psi_{1,2}(\mathbf{r})|^2 \int \frac{1}{1 + r'^6} d\mathbf{r}' \\ &= \gamma' |\psi_{1,2}(\mathbf{r})|^2, \end{aligned} \quad (12)$$

where $\gamma' = \frac{2\pi^2}{3^{3/2}} \tilde{C}_6$. Without external trap, assuming $\beta_{11} = \beta_{22}$, the matrix form of Eqs. (4) and (5) reads as

$$i \frac{\partial}{\partial t} \begin{pmatrix} \psi_1 \\ \psi_2 \end{pmatrix} = \begin{pmatrix} A & H_\kappa \\ -H_\kappa^* & B \end{pmatrix} \begin{pmatrix} \psi_1 \\ \psi_2 \end{pmatrix}, \quad (13)$$

where $A = -\nabla^2/2 + \alpha_1 |\psi_1|^2 + \alpha_2 |\psi_2|^2 + \Omega_R/2$, $B = -\nabla^2/2 + \alpha_1 |\psi_2|^2 + \alpha_2 |\psi_1|^2 - \Omega_R/2$, $H_\kappa = \kappa(q_x - iq_y)$, $\alpha_1 = (\beta_{11} + \gamma')$, and $\alpha_2 = (\beta_{12} + \gamma')$. When the Raman coupling strength $\Omega_R = 0$, the above GP equation (13) has the following plane wave solutions

$$\begin{pmatrix} \psi_1 \\ \psi_2 \end{pmatrix} = \frac{1}{\sqrt{2}} \begin{pmatrix} e^{i\theta\mathbf{k}} \\ -1 \end{pmatrix} e^{i(\mathbf{k}\cdot\mathbf{r} - \mu t)}, \quad (14)$$

where $\tan\theta_{\mathbf{k}} = k_x/k_y$ and $\mu = |\mathbf{k}|^2/2 - \kappa|\mathbf{k}| + (\alpha_1 + \alpha_2)/2$ is the chemical potential. Without loss of generality, we assume that the system moves along the x direction, that is, $\mathbf{k} = k\hat{x}$ with $k > 0$. According to the Bogoliubov theory, the perturbed state $\Psi_{1,2} = \psi_{1,2} + \delta\psi_{1,2}$ also satisfies the GP equation (13), where $\delta\psi_{1,2} = e^{i(kx - \mu t)} (u_{1,2}e^{-i\omega t} - v_{1,2}^*e^{i\omega t})$ with k and ω being the wave vector and the frequency of excitation. The mode functions $u_{1,2}$ and $v_{1,2}$ are determined by the Bogoliubov-de Gennes (BdG) equation [78–80]

$$M \begin{pmatrix} u_1 \\ u_2 \\ v_1 \\ v_2 \end{pmatrix} = \omega \begin{pmatrix} u_1 \\ u_2 \\ v_1 \\ v_2 \end{pmatrix}. \quad (15)$$

Here M is a 4×4 matrix,

$$M = \begin{pmatrix} H_{11} & H_{12} & -\frac{1}{2}\alpha_1 & \frac{1}{2}\alpha_2 \\ H_{21} & H_{22} & \frac{1}{2}\alpha_2 & -\frac{1}{2}\alpha_1 \\ \frac{1}{2}\alpha_1 & -\frac{1}{2}\alpha_2 & H_{33} & H_{34} \\ -\frac{1}{2}\alpha_2 & \frac{1}{2}\alpha_1 & H_{43} & H_{44} \end{pmatrix}, \quad (16)$$

with

$$\begin{aligned} H_{11} &= H_{22} = \frac{1}{2} [(q_x + k)^2 + q_y^2] + \frac{1}{2}\alpha_1 - \frac{k^2}{2} + \kappa k, \\ H_{33} &= H_{44} = -\frac{1}{2} [(q_x - k)^2 + q_y^2] - \frac{1}{2}\alpha_1 + \frac{k^2}{2} - \kappa k, \\ H_{12} &= \kappa(q_x - iq_y + k) - \frac{1}{2}\alpha_2, \\ H_{21} &= -\kappa(-q_x - iq_y - k) - \frac{1}{2}\alpha_2, \\ H_{34} &= -\kappa(-q_x - iq_y + k) + \frac{1}{2}\alpha_2, \\ H_{43} &= \kappa(q_x - iq_y - k) + \frac{1}{2}\alpha_2. \end{aligned}$$

In general, there are two groups of eigenvalues and the eigenvectors corresponding to the physical eigenvalues satisfy $\sum_{j=1,2} (|u_j|^2 - |v_j|^2) = 1$.

By numerically diagonalizing the BdG equation, we obtain the Bogoliubov excitation spectra as depicted in Figs. 4(a)-4(d). If the BECs satisfy $|\mathbf{k}| < \kappa$ (see Figs. 4(a1)-4(a3)), we find that some of the excitation spectra are imaginary (e.g., one can see the $\omega(q_y) = 0$ part of the lower branch in Fig. 4(a3), and the non-zero imaginary part of the excitation spectra are unable to be displayed here), which indicates that the BECs with $|\mathbf{k}| < \kappa$ are dynamically unstable [79, 80] and thus do not have superfluidity. In this case, our numerical simulation shows that the two branches of the excitation spectra come into contact each other at a single point in the region of $q_x < 0$. In addition, the system exists a critical value k_c , and when $|\mathbf{k}| > k_c$, the part of the excitation spectra become negative (e.g., see the lower branch in Figs. 4(b1) and 4(b2)), which means that the BECs with $|\mathbf{k}| > k_c$ suffer Landau instability [79–81] and have no superfluidity. In view of the conditions of dynamical instability

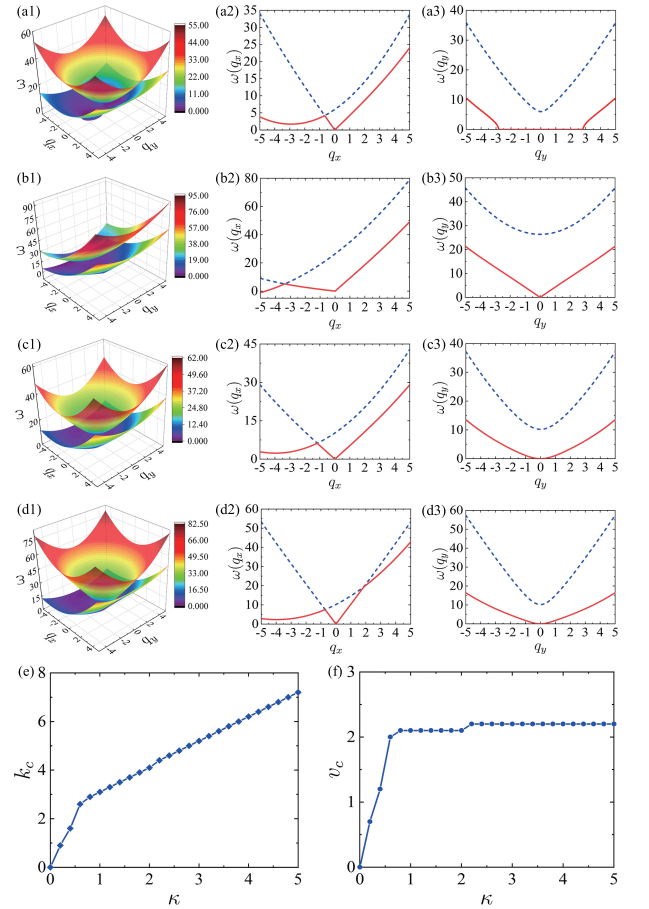


FIG. 4: (Color online) (a)-(d) Bogoliubov excitation spectra of a uniform 2D spin-orbit coupled Rydberg-dressed BEC. The left column denotes the 2D excitation spectrum, and the right two columns represent the excitation spectra along the x axis and the y axis, respectively. Here the dashed blue line represents the upper band of the excitation spectrum, and the solid red line denotes the lower band. (a1)-(a3) $k = 1$, $\kappa = 2$, $\gamma' = 20$, (b1)-(b3) $k = 6$, $\kappa = 2$, $\gamma' = 20$, (c1)-(c3) $k = 2$, $\kappa = 2$, $\gamma' = 20$, and (d1)-(d3) $k = 2$, $\kappa = 2$, $\gamma' = 100$. (e) The critical value k_c with respect to κ for $\gamma' = 20$. (f) The critical flowing velocity of the condensate v_c as a function of κ for $\gamma' = 20$. The other parameters are $\beta_{11} = 10$, $\beta_{12} = 5$, and $\Omega_R = 0$.

and Landau instability, we can conclude that only the BECs with $\kappa \leq |\mathbf{k}| \leq k_c$ have superfluidity, which has been verified in our numerical computations. The effect of the Rydberg interaction on the excitation spectrum in the superfluid regime ($\kappa \leq |\mathbf{k}| \leq k_c$) is shown in Figs. 4(c1)-4(c3) and Figs. 4(d1)-4(d3). With the reduction of $|\mathbf{k}|$, the lower branch of the spectra along the y direction becomes softer (see Fig. 4(b3) and Fig. 4(c3)). Intriguingly, for strong Rydberg interaction, the two branches of the excitation spectra along the x axis contact with each other at two points on either side of $q_x = 0$ (Fig. 4(d2)), which is remarkably different from the case of conventional spin-orbit coupled BEC [78] and allows to be observed in the future cold-atom experiments concerning

on the Rydberg-dressed BECs with SOC.

Furthermore, the critical value k_c as a function of the SOC strength κ for $\gamma' = 20$ is given in Fig. 4(e). When $\kappa < 1$, the critical value k_c first grows rapidly and then increases relatively slowly. when $\kappa > 1$, the k_c - κ relationship approaches a linear growth. For the case of $\kappa \leq |\mathbf{k}| \leq k_c$, the BECs are superfluids with super-flow speeds being smaller than the corresponding critical flowing velocity $v_c = k_c - \kappa$ [78]. Fig. 4(f) shows the critical flowing velocity v_c with respect to the SOC strength κ for $\gamma' = 20$. The critical flowing velocity of superfluid is one of the key features of spin-orbit coupled BECs, where the SOC breaks the Galilean invariance of the BECs. We find that the critical flowing velocity v_c of the condensate increases rapidly from zero for weak SOC. When the SOC strength κ increases to about 0.8, the critical flowing velocity gradually tends to a stable value. If κ continues to increase and reaches approximately 2.2, v_c suddenly rises to a new stable value. With the further increase of κ , v_c remains at the second new stable value.

D. Dissipative time crystal

In Sec. III. A, we have discussed the ground-state properties of BECs with Raman-induced SOC and Rydberg interactions in a harmonic trap. Now we investigate the rotational dynamic behaviors of the system, where it is necessary to take into account dissipation. As a matter of fact, the dissipation in rotating BECs is universal and inevitable in real cold-atom experiments. Here we use a phenomenological dissipation model [71, 73, 82] to study the rotating dynamics of the system. Moreover, Rydberg atoms are well controllable, which provides a suitable platform for the study of continuous time crystal (CTC), and the CTC has an order parameter with self-sustained oscillations [64, 65, 83]. Therefore, the dynamic process of the system can be revealed by examining the change of angular momentum with time. We are interested in exploring whether a similar CTC exists in this system. According to the phenomenological dissipation model [71, 73, 82], the nonlinear coupled GP equations (4)-(5) are transformed as follows

$$\begin{aligned}
 (i - \lambda) \frac{\partial \psi_1}{\partial t} = & \left[-\frac{1}{2} \nabla^2 + V(\mathbf{r}) + \beta_{11} |\psi_1|^2 + \beta_{12} |\psi_2|^2 \right. \\
 & + \frac{\Omega_R}{2} + \int U_{11}(\mathbf{r} - \mathbf{r}') |\psi_1(\mathbf{r}')|^2 d\mathbf{r}' \\
 & + \int U_{12}(\mathbf{r} - \mathbf{r}') |\psi_2(\mathbf{r}')|^2 d\mathbf{r}' - \Omega_r L_z \left. \right] \psi_1 \\
 & - \kappa (i\partial_x + \partial_y) \psi_2 - \frac{\delta}{2} \psi_2, \quad (17)
 \end{aligned}$$

$$\begin{aligned}
 (i - \lambda) \frac{\partial \psi_2}{\partial t} = & \left[-\frac{1}{2} \nabla^2 + V(\mathbf{r}) + \beta_{22} |\psi_2|^2 + \beta_{21} |\psi_1|^2 \right. \\
 & - \frac{\Omega_R}{2} + \int U_{22}(\mathbf{r} - \mathbf{r}') |\psi_2(\mathbf{r}')|^2 d\mathbf{r}' \\
 & + \int U_{21}(\mathbf{r} - \mathbf{r}') |\psi_1(\mathbf{r}')|^2 d\mathbf{r}' - \Omega_r L_z \left. \right] \psi_2 \\
 & - \kappa (i\partial_x - \partial_y) \psi_1 - \frac{\delta}{2} \psi_1. \quad (18)
 \end{aligned}$$

Here we choose the dissipation parameter $\lambda = 0.005$, which corresponds to a temperature of around $0.003T_c$. A small dissipation parameter λ slows the relaxation time to allow for detailed observation. But the variation of nonzero λ does not change the dynamics of topological defect formation and the ultimate steady structure of the rotating system. We select four typical ground states as the initial states of dynamical evolution, and the specific parameters are (a) $\tilde{C}_6 = 250$, $\kappa = 4$, $\Omega_R = 16$, (b) $\tilde{C}_6 = 1500$, $\kappa = 4$, $\Omega_R = 0$, (c) $\tilde{C}_6 = 1500$, $\kappa = 4$, $\Omega_R = 10$, and (d) $\tilde{C}_6 = 1500$, $\kappa = 7$, $\Omega_R = 10$ for $\beta_{11} = \beta_{22} = 100$ and $\beta_{12} = 200$. Note that the parameter values of (b), (c) and (d) are the same as those of (V), (VI) and (VII) in Fig. 2(c), respectively. Figs. 5(a)-5(d) show the temporal evolution of the mean orbital angular momentum per atom $\langle L_z \rangle$ and typical density distribution of the system after the harmonic trap begins to rotate suddenly with $\Omega_r = 0.6$.

In Fig. 5(a), we find that the amplitude of $\langle L_z \rangle$ gradually changes from an initial attenuation to a regular periodic persistent oscillation over time. This result is dramatically different from that of the spin-orbit coupled BECs without soft-core long-range Rydberg interactions [84]. For the latter case, the mean orbital angular momentum per atom increases rapidly with the time evolution and then gradually approaches a maximum equilibrium value. The main reason for this oscillation is that the long-range interactions induced by Rydberg dressing involve the coexistence and competition between multiple Rydberg states in the rotational dynamical system [65]. During the dynamical evolution, the system evolves from a multi-layer concentric toroidal stripe phase to an Anderson-Toulouse coreless vortex. However, when the system begins to rotate with a supersolid phase as the initial state, the evolution of the orbital angular momentum over time is shown in Figs. 5(b)-5(d). If the SOC type in the system is Rashba SOC as shown in Fig. 5(b), the results indicate that $\langle L_z \rangle$ first increases rapidly with the time evolution, then decreases in the form of damping oscillation after reaching the peak, and finally oscillates with a small amplitude near an equilibrium value.

For the system with Raman-induced SOC as displayed in Fig. 5(c), we find that a particular structural transition occurs at $t \approx 315$ before which $\langle L_z \rangle$ experiences irregular quasi-periodic alternating complex oscillations composed of downward damping oscillations and upward amplification oscillations, and after which $\langle L_z \rangle$ increases in a quasi-periodic oscillation pattern until the oscillation is stable. The quasi-periodic oscillation in the process of

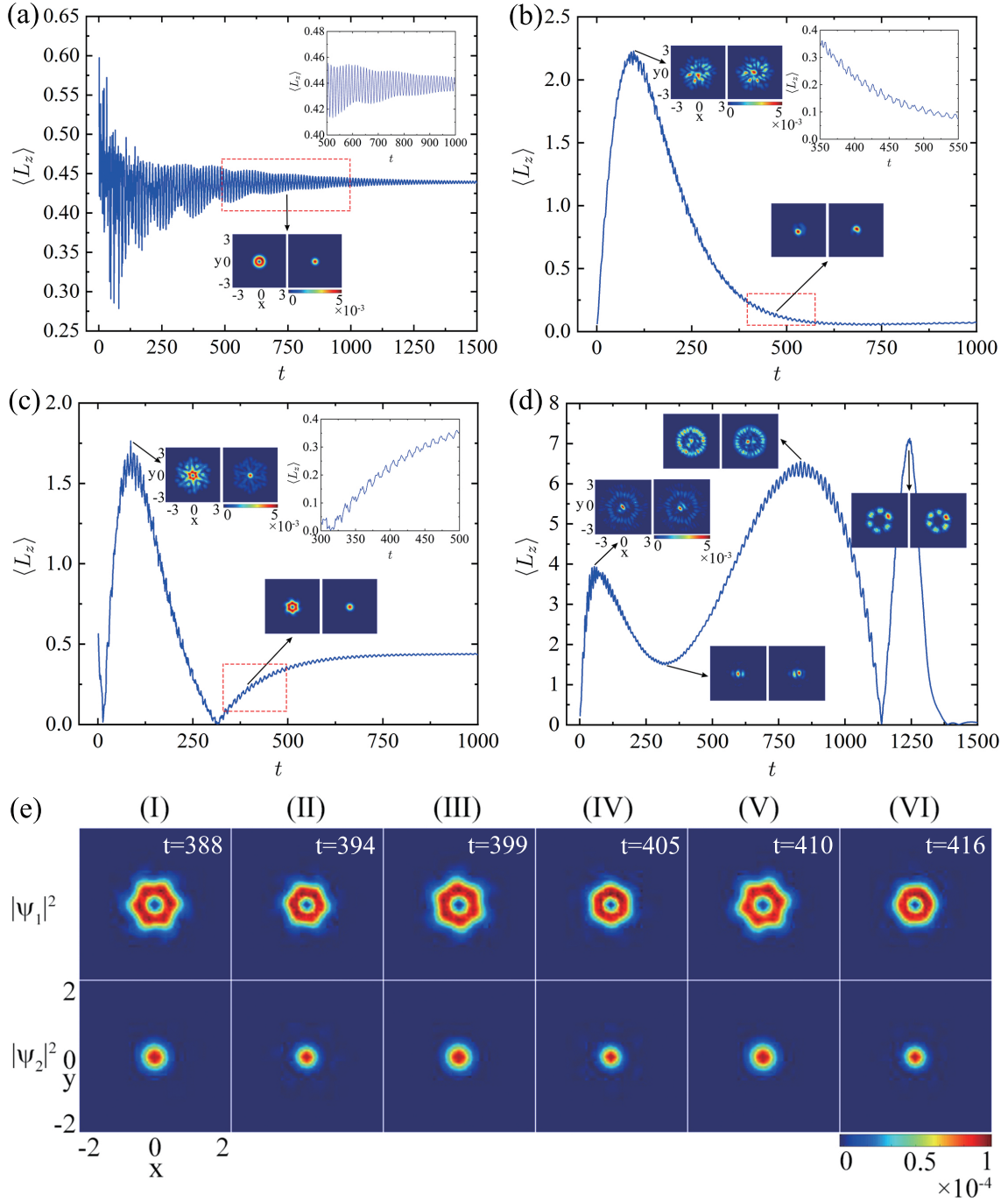


FIG. 5: (Color online) (a)–(d) Temporal evolution of the average orbital angular momentum per atom $\langle L_z \rangle$ for (a) $\tilde{C}_6 = 250$, $\kappa = 4$, $\Omega_R = 16$, (b) $\tilde{C}_6 = 1500$, $\kappa = 4$, $\Omega_R = 0$, (c) $\tilde{C}_6 = 1500$, $\kappa = 4$, $\Omega_R = 10$, and (d) $\tilde{C}_6 = 1500$, $\kappa = 7$, $\Omega_R = 10$. The insets in the upper right corners of panels (a)–(c) illustrate the local enlargements of the red dotted frames, respectively. The component density distributions at specific moments are shown in panels (a)–(d). (e) The temporal evolution of the density distribution corresponding to the red dotted frame in panel (c). Here t and $\langle L_z \rangle$ are in units of τ and \hbar , respectively. The unit length is R_c .

dynamical evolution is strong evidence of the time crystal. Fig. 5(e) shows the typical dynamics of the density distribution, where $\tilde{C}_6 = 1500$, $\kappa = 4$, $\Omega_R = 10$, and the representative time points are (I) $t = 388$, (II) $t = 394$, (III) $t = 399$, (IV) $t = 405$, (V) $t = 410$, and (VI) $t = 416$.

We observe that the distribution area of the condensate varies periodically with time, and the condensate area achieves the maximum at the trough of $\langle L_z \rangle$ oscillation and the minimum at the crest of $\langle L_z \rangle$ oscillation. As is well known, if a quantum state is an eigenstate of the an-

angular momentum operator L_z , the expected values $\langle L_x \rangle$ and $\langle L_y \rangle$ of the angular momentum operators L_x and L_y will both be zero. Obviously, the system spinor wave function during the dynamical evolution is not the eigenstate of the angular momentum operator L_z , therefore the expected values $\langle L_x \rangle$ and $\langle L_y \rangle$ are non-zero. The dissipation considered here is weak, so its influence on the angular momentum in a short time can be ignored. Physically, for a constant rotation frequency, when the z component of the angular momentum decreases, the x and y components of the angular momentum increase, and vice versa. $\langle L_z \rangle$ is small at the trough and large at the crest, which means that $\langle L_x \rangle$ and $\langle L_y \rangle$ are large at the trough and small at the crest. This point can explain the periodic change of the condensate area in the x - y plane. The continuous periodic changes of the condensate are significant characteristics of CTC. Here the density distribution of the CTC turns out to be a phase separation structure and the chiral symmetry of the system is broken. Thus the appearance of quasi-periodic oscillation part of the system indicates the existence of chiral CTC. In Fig. 5(d), the results show that the system has multiple transition points due to the larger SOC strength and the more complex density distribution of the SWSS phase in the selected initial state. Moreover, the variation of the angular momentum input is affected by the complex competition among nonlinear contact interactions, SOC, Rydberg interactions and rotation during the process of dynamical evolution.

E. Experimental feasibility

Recently, the realization of artificial SOC offers an excellent platform with full controllability for exploring novel macroscopic quantum phenomena and quantum topological states. In particular, one-dimensional (1D) [31], 2D [55] and 3D [56] Raman SOC in BECs have been experimentally achieved by Raman coupling that flips atom spins (pseudospins) and transfers momentum simultaneously, which provides a reliable experimental basis for realizing our results. One can consider alkali atoms like ^{87}Rb atoms, where the ground-state electronic structure is $^2S_{1/2}$ with $S = 1/2$ and $I = 3/2$. In previous experimental schemes, the two spin states $|1, 0\rangle$ and $|1, -1\rangle$ of ^{87}Rb atom were usually chosen and the atomic system was regarded as a pseudospin-1/2 system [31]. The Raman-induced SOC can be induced by two counter-propagating Raman laser lights along \hat{x} [32]. In addition, one can use the Rydberg dressing technology to create the soft-core long-range interactions in the ^{87}Rb platform [16, 85, 86], and apply the Rydberg lasers to the system that have achieved Raman-induced SOC. Both the two hyperfine ground states $|1, 0\rangle$ and $|1, -1\rangle$ are selected and they can be optically coupled to the same excited $60S_{1/2}$ Rydberg states by a two-photon process with the Rabi frequency Ω and detuning Δ as shown in Fig. 1 of Ref. [16]. The system can be seen as an ef-

fective two-level atom with a Rabi frequency $\Omega_1 = \frac{\Omega_\alpha \Omega_\beta}{2\Delta_1}$ ($\Omega_2 = \frac{\Omega_\beta \Omega_\alpha}{2\Delta_1}$) and detuning $\Delta = \Delta_1 + \Delta_2$, where $\Omega_{\alpha,\beta}$ is the Rabi frequencies and $\Delta_{1,2}$ ($\Delta_1 = \Delta_2$) is the detuning in the two hyperfine ground states. For the case of weak coupling ($\Omega_{1,2} \ll \Delta$), the soft-core long-range interactions modified by Rydberg dressing is expressed as $U_{jl}(\mathbf{r}) = \tilde{C}_6^{(jl)} / (R_c^6 + |\mathbf{r}|^6)$ [16, 48].

IV. CONCLUSIONS

In summary, we have investigated the ground-state properties, excitation spectra and rotational dynamic behaviors of quasi-2D two-component BECs with Raman-induced SOC and Rydberg interactions. We show that in the absence of Raman coupling (i.e., for the case of Rashba SOC) the ground state of the system sustains a mirror symmetric supersolid phase with skyrmion-antiskyrmion lattice pair. Whereas the Raman-induced SOC can lead to the formation of a novel chiral supersolid phase with a helical antiskyrmion lattice in two-component BECs with balanced Rydberg interactions in a harmonic trap. We present two ground-state phase diagrams in which one is spanned by the Rydberg interaction strength and the SOC strength, and another is with respect to the Rydberg interaction strength and the Raman coupling strength. The system exhibits a rich variety of quantum phases besides the mirror symmetric supersolid phase and the chiral supersolid phase, such as stripe supersolid phase, toroidal stripe phase with a central Anderson-Toulouse coreless vortex, checkerboard supersolid phase, and standing-wave supersolid phase, which can be achieved by adjusting the Rydberg interaction strength, the Raman coupling strength, or the SOC strength. In addition, both rotation and in-plane quadrupole magnetic field can break the chiral supersolid phase and make the ground-state structure develop towards a miscible phase.

Furthermore, we have analyzed the Bogoliubov excitation spectra and stability features of the quasi-2D two-component BECs with Raman-induced SOC and Rydberg interactions in free space by solving the Bogoliubov-de Gennes equation. When the wave number $|\mathbf{k}|$ satisfies $|\mathbf{k}| < \kappa$ or $|\mathbf{k}| > \kappa_c$ (critical value), the system suffers dynamical instability or Landau instability, respectively, and has no superfluidity. For the superfluid condensates, the lower branch of the excitation spectra along the y direction becomes softer when the wave number decreases. In particular, for the case of strong Rydberg interaction, the two branches of the excitation spectra along the x axis contact with each other at two points on either side of $q_x = 0$. Moreover, we have discussed the rotating dynamics of Rydberg-dressed BECs with Raman-induced SOC in a harmonic trap by using a phenomenological dissipation model. We find that when the initial state is a chiral supersolid phase the rotating system supports dissipative continuous time crystals. These findings in

the present work enrich our new knowledge and understanding for the peculiar matter states such as supersolid, superfluid, and time crystal in cold atom physics and condensed matter physics, which allow to be tested and observed in the future experiments.

Acknowledgments

This work was supported by the National Natural Science Foundation of China (Grant No. 11475144), Hebei

Natural Science Foundation (Grant Nos. A2022203001, A2019203049 and A2015203037), and Research Foundation of Yanshan University (Grant No. B846).

-
- [1] A. J. Leggett, *Phys. Rev. Lett.* **25**, 1543 (1970).
 [2] G. V. Chester, *Phys. Rev. A* **2**, 256 (1970).
 [3] M. Boninsegni and N. V. Prokof'ev, *Rev. Mod. Phys.* **84**, 759 (2012).
 [4] E. Kim and M. H. W. Chan, *Nature (London)* **427**, 225 (2004).
 [5] D. Y. Kim and M. H. W. Chan, *Phys. Rev. Lett.* **109**, 155301 (2012).
 [6] J.-R. Li, J. Lee, W. Huang, S. Burchesky, B. Shteynas, F. Ç. Top, A. O. Jamison, and W. Ketterle, *Nature (London)* **543**, 91 (2017).
 [7] K. T. Geier, G. I. Martone, P. Hauke, W. Ketterle, and S. Stringari, *Phys. Rev. Lett.* **130**, 156001 (2023).
 [8] L. Tanzi, E. Lucioni, F. Famà, J. Catani, A. Fioretti, C. Gabbanini, R. N. Bisset, L. Santos, and G. Modugno, *Phys. Rev. Lett.* **122**, 130405 (2019).
 [9] F. Böttcher, J.-N. Schmidt, M. Wenzel, J. Hertkorn, M. Guo, T. Langen, and T. Pfau, *Phys. Rev. X* **9**, 011051 (2019).
 [10] L. Chomaz, D. Petter, P. Ilzhöfer, G. Natale, A. Trautmann, C. Politi, G. Durastante, R. M. W. van Bijnen, A. Patscheider, M. Sohmen, M. J. Mark, and F. Ferlaino, *Phys. Rev. X* **9**, 021012 (2019).
 [11] L. Tanzi, J. G. Maloberti, G. Biagioni, A. Fioretti, C. Gabbanini, and G. Modugno, *Science* **371**, 1162 (2021).
 [12] B. T. E. Ripley, D. Baillie, and P. B. Blakie, *Phys. Rev. A* **108**, 053321 (2023).
 [13] L. Chomaz, I. Ferrier-Barbut, F. Ferlaino, B. Laburthe-Tolra, B. L. Lev, and T. Pfau, *Rep. Prog. Phys.* **86**, 026401 (2023).
 [14] S. Wessel and M. Troyer, *Phys. Rev. Lett.* **95**, 127205 (2005).
 [15] R. Landig, L. Hruby, N. Dogra, M. Landini, R. Mottl, T. Donner, and T. Esslinger, *Nature (London)* **532**, 476 (2016).
 [16] N. Henkel, R. Nath, and T. Pohl, *Phys. Rev. Lett.* **104**, 195302 (2010).
 [17] F. Cinti, P. Jain, M. Boninsegni, A. Micheli, P. Zoller, and G. Pupillo, *Phys. Rev. Lett.* **105**, 135301 (2010).
 [18] N. Henkel, F. Cinti, P. Jain, G. Pupillo, and T. Pohl, *Phys. Rev. Lett.* **108**, 265301 (2012).
 [19] C.-H. Hsueh, T.-C. Lin, T.-L. Horng, and W. C. Wu, *Phys. Rev. A* **86**, 013619 (2012).
 [20] J. Zeiher, R. van Bijnen, P. Schauß, S. Hild, J. Choi, T. Pohl, I. Bloch, and C. Gross, *Nat. Phys.* **12**, 109 (2016).
 [21] I. Seydi, S. H. Abedinpour, R. E. Zillich, R. Asgari, and B. Tanatar, *Phys. Rev. A* **101**, 013628 (2020).
 [22] D. S. Petrov, *Phys. Rev. Lett.* **115**, 155302 (2015).
 [23] F. Wächtler and L. Santos, *Phys. Rev. A* **93**, 061603(R) (2016).
 [24] I. Ferrier-Barbut, H. Kadau, M. Schmitt, M. Wenzel, and T. Pfau, *Phys. Rev. Lett.* **116**, 215301 (2016).
 [25] D. Baillie and P. B. Blakie, *Phys. Rev. Lett.* **121**, 195301 (2018).
 [26] S. M. Rocuzzo, A. Gallemí, A. Recati, and S. Stringari, *Phys. Rev. Lett.* **124**, 045702 (2020).
 [27] X. Su, W. Dai, T. Li, J. Wang, and L. Wen, *Chaos Solitons Fractals* **184**, 114979 (2024).
 [28] J. Hertkorn, J.-N. Schmidt, M. Guo, F. Böttcher, K. S. H. Ng, S. D. Graham, P. Uerlings, T. Langen, M. Zwierlein, and T. Pfau, *Phys. Rev. Res.* **3**, 033125 (2021).
 [29] L. E. Young-S. and S. K. Adhikari, *Phys. Rev. A* **105**, 033311 (2022).
 [30] J. Hertkorn, J.-N. Schmidt, M. Guo, F. Böttcher, K. S. H. Ng, S. D. Graham, P. Uerlings, H. P. Buchler, T. Langen, M. Zwierlein, and T. Pfau, *Phys. Rev. Lett.* **127**, 155301(2021).
 [31] Y.-J. Lin, K. Jiménez-García, and I. B. Spielman, *Nature (London)* **471**, 83 (2011).
 [32] H. Zhai, *Rep. Prog. Phys.* **78**, 026001 (2015).
 [33] Y. Zhang, L. Mao, and C. Zhang, *Phys. Rev. Lett.* **108**, 035302 (2012).
 [34] H. Wang, L. Wen, H. Yang, C. Shi, and J. Li, *J. Phys. B: At. Mol. Opt. Phys.* **50**, 155301 (2017).
 [35] W. Han, G. Juzeliunas, W. Zhang, and W. M. Liu, *Phys. Rev. A* **91**, 013607 (2015).
 [36] S. Sinha, R. Nath, and L. Santos, *Phys. Rev. Lett.* **107**, 270401 (2011).
 [37] J. Hu, Q. Wang, X. Su, Y. Zhang, and L. Wen, *Results Phys.* **34**, 105238 (2022).
 [38] X.-Q. Xu and J. H. Han, *Phys. Rev. Lett.* **107**, 200401 (2011).
 [39] J. Radić, T. A. Sedrakyan, I. B. Spielman, and V. Galitski, *Phys. Rev. A* **84**, 063604 (2011).
 [40] A. Aftalion and P. Mason, *Phys. Rev. A* **88**, 023610 (2013).
 [41] Y. Xu, Y. Zhang, and B. Wu, *Phys. Rev. A* **87**, 013614 (2013).
 [42] H. Sakaguchi, B. Li, and B. A. Malomed, *Phys. Rev. E* **89**, 032920 (2014).
 [43] H. Hu, B. Ramachandhran, H. Pu, and X.-J. Liu, *Phys. Rev. Lett.* **108**, 010402 (2012).
 [44] E. I. Rashba and V. I. Sheka, *Fiz. Tverd. Tela* **2**, 162 (1959).

- [45] G. Dresselhaus, *Phys. Rev.* **100**, 580 (1955).
- [46] N. Goldman, G. Juzeliunas, P. Ohberg, and I. B. Spielman, *Rep. Prog. Phys.* **77**, 126401 (2014).
- [47] H. Lü, S.-B. Zhu, J. Qian, and Y.-Z. Wang, *Chin. Phys. B* **24**, 090308 (2015).
- [48] W. Han, X.-F. Zhang, D.-S. Wang, H.-F. Jiang, W. Zhang, and S.-G. Zhang, *Phys. Rev. Lett.* **121**, 030404 (2018).
- [49] H. Lyu and Y. Zhang, *Phys. Rev. A* **102**, 023327 (2020).
- [50] X.-F. Zhang, L. Wen, L.-X. Wang, G.-P. Chen, R.-B. Tan, and H. Saito, *Phys. Rev. A* **105**, 033306 (2022).
- [51] C. Kallin and J. Berlinsky, *Rep. Prog. Phys.* **79**, 054502 (2016).
- [52] S.-H. Yang, R. Naaman, Y. Paltiel, and S. S. P. Parkin, *Nat. Rev. Phys.* **3**, 328 (2021).
- [53] A. Szasz, J. Motruk, M. P. Zaletel, and J. E. Moore, *Phys. Rev. X* **10**, 021042 (2020).
- [54] L. Wang, A. M. Urbas, and Q. Li, *Adv. Mater.* **32**, 1801335 (2020).
- [55] Z. Wu, L. Zhang, W. Sun, X.-T. Xu, B.-Z. Wang, S.-C. Ji, Y. Deng, S. Chen, X.-J. Liu, and J.-W. Pan, *Science* **354**, 83 (2016).
- [56] Z.-Y. Wang, X.-C. Cheng, B.-Z. Wang, J.-Y. Zhang, Y.-H. Lu, C.-R. Yi, S. Niu, Y. Deng, X.-J. Liu, S. Chen, and J.-W. Pan, *Science* **372**, 271 (2021).
- [57] F. Wilczek, *Phys. Rev. Lett.* **109**, 160401 (2012).
- [58] K. Sacha and J. Zakrzewski, *Rep. Prog. Phys.* **81**, 016401 (2018).
- [59] B. Huang, Y.-H. Wu, and W. V. Liu, *Phys. Rev. Lett.* **120**, 110603 (2018).
- [60] J. Rovny, R. L. Blum, and S. E. Barrett, *Phys. Rev. Lett.* **120**, 180603 (2018).
- [61] H. Keßler, P. Kongkhambut, C. Georges, L. Mathey, J. G. Cosme, and A. Hemmerich, *Phys. Rev. Lett.* **127**, 043602 (2021).
- [62] J. Zhang, P. W. Hess, A. Kyprianidis, P. Becker, A. Lee, J. Smith, G. Pagano, I.-D. Potirniche, A. C. Potter, A. Vishwanath, N. Y. Yao, and C. Monroe, *Nature (London)* **543**, 217 (2017).
- [63] S. Choi, J. Choi, R. Landig, G. Kucsko, H. Zhou, J. Isoya, F. Jelezko, S. Onoda, H. Sumiya, V. Khemani, C. Keyserlingk, N. Y. Yao, E. Demler, and M. D. Lukin, *Nature (London)* **543**, 221 (2017).
- [64] P. Kongkhambut, J. Skulte, L. Mathey, J. G. Cosme, A. Hemmerich, and H. Keßler, *Science* **377**, 670 (2022).
- [65] X. Wu, Z. Wang, F. Yang, R. Gao, C. Liang, M. K. Tey, X. Li, T. Pohl, and L. You, *Nat. Phys.* **20**, 1389 (2024).
- [66] K. Kasamatsu, M. Tsubota, and M. Ueda, *Phys. Rev. A* **71**, 043611 (2005).
- [67] T. H. R. Skyrme, *Nucl. Phys.* **31**, 556 (1962).
- [68] N. D. Mermin and T.-L. Ho, *Phys. Rev. Lett.* **36**, 594 (1976).
- [69] N. Nagaosa and Y. Tokura, *Nature Nanotech.* **8**, 899 (2013).
- [70] P. W. Anderson and G. Toulouse, *Phys. Rev. Lett.* **38**, 508 (1977).
- [71] L. Wen, H. Xiong, and B. Wu, *Phys. Rev. A* **82**, 053627 (2010).
- [72] L. Wen, Y. Qiao, Y. Xu, and L. Mao, *Phys. Rev. A* **87**, 033604 (2013).
- [73] L. Wen and J. Li, *Phys. Rev. A* **90**, 053621 (2014).
- [74] M. W. Ray, E. Ruokokoski, S. Kandel, M. Möttönen, and D. S. Hall, *Nature (London)* **505**, 657 (2014).
- [75] X. Li, Q. Wang, H. Wang, C. Shi, M. Jardine, and L. Wen, *J. Phys. B: At. Mol. Opt. Phys.* **52**, 155302 (2019).
- [76] R. K. Kumar, P. Muruganandam, L. Tomio, and A. Gammal, *J. Phys. Commun.* **1**, 035012 (2017).
- [77] R. K. Kumar, L. Tomio, and A. Gammal, *Phys. Rev. A* **99**, 043606 (2019).
- [78] Q. Zhu, C. Zhang, and B. Wu, *EPL* **100**, 50003 (2012).
- [79] B. Wu and Q. Niu, *Phys. Rev. A* **64**, 061603(R) (2001).
- [80] B. Wu and Q. Niu, *New J. Phys.* **5**, 104 (2003).
- [81] W.-L. Xia, L. Chen, T.-T. Li, Y. Zhang, and Q. Zhu, *Phys. Rev. A* **107**, 053302 (2023).
- [82] K. Kasamatsu, M. Tsubota, and M. Ueda, *Phys. Rev. A* **67**, 033610 (2003).
- [83] M. Krishna, P. Solanki, M. Hajdušek, and S. Vinjanampathy, *Phys. Rev. Lett.* **130**, 150401 (2023).
- [84] Q. Wang, J. Hu, X. Su, and L. Wen, *Results Phys.* **20**, 103755 (2021).
- [85] C.-H. Hsueh, Y.-C. Tsai, K.-S. Wu, M.-S. Chang, and W. C. Wu, *Phys. Rev. A* **88**, 043646 (2013).
- [86] R. Heidemann, U. Raitzsch, V. Bendkowsky, B. Butscher, R. Löw, and T. Pfau, *Phys. Rev. Lett.* **100**, 033601 (2008).